

# Self-supervised Physics-Informed Manipulation of Deformable Linear Objects with Non-negligible Dynamics

Youyuan Long<sup>1,2</sup>, Gokhan Solak<sup>1</sup>, Sara Zeynalpour<sup>1</sup>, Heng Zhang<sup>1,2</sup>, and Arash Ajoudani<sup>1</sup>

**Abstract**—We address dynamic manipulation of deformable linear objects by presenting **SPiD**, a physics-informed self-supervised learning framework that couples an accurate deformable object model with an augmented self-supervised training strategy. On the modeling side, we extend a mass-spring model to more accurately capture object dynamics while remaining lightweight enough for high-throughput rollouts during self-supervised learning. On the learning side, we train a neural controller using a task-oriented cost, enabling end-to-end optimization through interaction with the differentiable object model. In addition, we propose a self-supervised DAgger variant that detects distribution shift during deployment and performs offline self-correction to further enhance robustness without expert supervision. We evaluate our method primarily on the rope stabilization task, where a robot must bring a swinging rope to rest as quickly and smoothly as possible. Extensive experiments in both simulation and the real world demonstrate that the proposed controller achieves fast and smooth rope stabilization, generalizing across unseen initial states, rope lengths, masses, non-uniform mass distributions, and external disturbances. Additionally, we develop an affordable markerless rope perception method, and demonstrate that our controller maintains performance with noisy and low-frequency state updates. Furthermore, we demonstrate the generality of the framework by extending it to the rope trajectory tracking task. Overall, SPiD offers a data-efficient, robust, and physically grounded framework for dynamic manipulation of deformable linear objects, featuring strong sim-to-real generalization.

## I. INTRODUCTION

With the advances in robot autonomy and hardware, robots are now being deployed in human-centered environments such as homes, shopping malls, and hospitals. These environments contain a wide variety of deformable objects, such as ropes, tubes, clothes, paper, and sponges [1], [2]. The ability to manipulate such deformable objects is therefore of great practical importance for service and domestic robots. However, tasks that are trivial for humans remain highly challenging for robots. The difficulty mainly arises from the following factors.

First of all, unlike rigid bodies, deformable objects exhibit infinite-dimensional degrees of freedom and can easily deform under even small external forces or disturbances. Moreover, their deformation behavior is highly nonlinear and often involves coupled physical effects such as tension,

This work was supported by the Horizon Europe Project TORNADO (GA 101189557).

<sup>1</sup>Human-Robot Interfaces and Interaction Lab, Istituto Italiano di Tecnologia, Genova, Italy (e-mail: youyuan.long@iit.it; gokhan.solak@iit.it; sara.zeynalpour@iit.it; heng.zhang@iit.it; arash.ajoudani@iit.it).

<sup>2</sup>Ph.D. program of national interest in Robotics and Intelligent Machines (DRIM) and Università di Genova, Genoa, Italy.

bending, and twisting [1]. Consequently, accurately modeling their dynamics is significantly more complex than that of rigid-body systems.

Furthermore, in contrast to quasi-static manipulation, dynamic manipulation (high-velocity actions) refers to control and interaction scenarios in which inertial and time-varying effects play a dominant role in the object’s motion [3], often resulting in fast and pronounced deformations for deformable objects. Such manipulation is highly challenging due to the complex dynamics of deformable objects, strict control latency requirements, and a significant sim-to-real gap. As a result, many traditional optimization-based approaches struggle to achieve real-time performance and stability [1].

Due to these challenges, many researchers have turned to data-driven approaches for deformable object manipulation, such as learning dynamic models from visual data [4], [5] or training controllers from human demonstrations [6]. However, these methods typically require large amounts of high-quality data and often suffer from limited generalization capability.

To address these challenges, we propose the **SPiD** (Self-supervised Physics-informed learning for Deformable object manipulation) framework, which consists of two main components: physics-informed modeling and learning-based control. As an initial and principled instantiation of deformable object manipulation, we focus on rope manipulation, which captures many of the core difficulties of deformable interaction, such as high-dimensional continuous state spaces, nonlinear dynamics, and strong coupling between contact forces and global object configuration. In SPiD, a *differentiable rope dynamics model* lies at the core of the framework. The model parameters are identified using differentiable physics-based system identification (Sec. III-B). This model is computationally efficient yet remains highly nonlinear and high-dimensional (in our simulation, the rope consists of 21 mass points, resulting in a 126-dimensional state space). Under such conditions, traditional model-based optimization methods, such as MPC, are prone to local optima and difficult to deploy in real time due to their iterative computation and nonconvex dynamics [7], [8]. Instead, we leverage the differentiable physics model to *train a neural controller offline through self-supervision*, shifting the heavy computation to the training phase while enabling fast online control execution via efficient neural network matrix operations. This framework highlights two key features:

- **Dynamic physical modeling:** To capture the dynamic characteristics of rope motion, we extend the con-

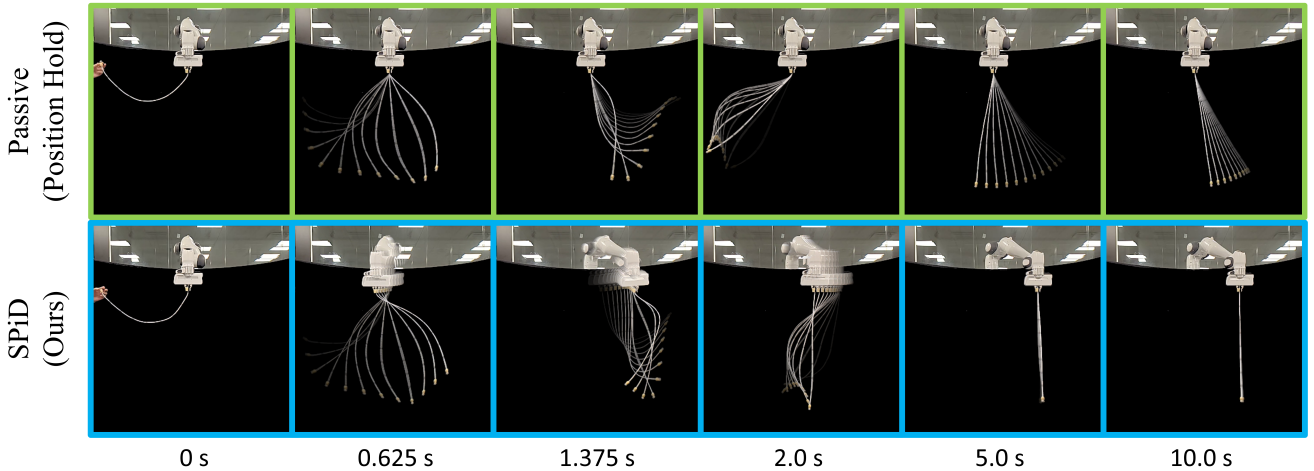


Fig. 1: **Dynamic manipulation for rope stabilization.** Comparison between our controller and the passive case (where the robot arm holds its position). Each subfigure shows the rope motion at the current time, with 12 ghosted frames traced backward at 37.5 ms intervals—the fainter the trace, the earlier the time. Our controller actively computes actions that minimize the rope’s energy in real time, achieving superior performance, whereas the passive case relies solely on air resistance to dissipate energy.

ventional mass–spring model by introducing additional damping terms and deriving their numerically stable analytical expressions. Our experiments (Sec. V-A) demonstrate that our model more accurately captures the rope’s dynamic behavior than the previous approach in [9].

- **Augmented self-supervised learning strategy:** By designing a task-oriented loss function and allowing the neural controller to interact with the deformable linear object (DLO) model, we train a control policy by minimizing this loss through gradient-based optimization. This differentiable-physics approach eliminates the need for expert demonstrations and shifts the major computational burden to the offline training phase. To mitigate the sim-to-real gap, we inject noise into the identified model parameters, enabling the controller to achieve robust performance across objects with different physical properties. Furthermore, we propose a *self-supervised DAgger* mechanism (Sec. III-C) to address the distribution-shift problem in the self-supervised setting. This mechanism enables the controller to continually refine its policy under real-world feedback without relying on expert demonstrations.

To validate our approach, we focus on the rope stabilization task, which involves controlling one end of the rope to bring an initially swinging rope to rest as quickly as possible. This task is highly dynamic and practically significant in various applications, such as industrial hoisting operations, aerial hoist rescue, and UAV payload delivery. However, it remains an underexplored problem. Most existing studies have focused on crane systems [10]–[12], cable-suspended UAV systems [13]–[15], or elevator rope sway control [16]. In these works, the rope is often simplified as a single- or double-pendulum model with restricted swing angles, and in some cases, the rope motion is further constrained to a two-

dimensional plane. Although such simplifications may be reasonable for specific scenarios, they significantly weaken the inherent three-dimensional flexibility and dynamic complexity of the rope as a deformable body. In contrast, in our task, the rope is initialized at a large swing angle, exhibiting fast and rich dynamic behaviors during its return phase, and the entire process occurs in three-dimensional space (Fig. 1).

Our framework is validated in four perspectives: 1) *Physics modeling* contribution is evaluated in comparison to the closest modeling baseline [9], demonstrating that it significantly improves the accuracy of long horizon prediction of rope motion. 2) *Learning and control* aspect is evaluated through the rope stabilization experiments, achieving agile manipulation with superior performance in comparison to the baseline [10]. 3) *Robustness* aspect is validated through rope stabilization using a single-camera (markerless) perception system. For this purpose, we developed a data-driven markerless perception method and analyzed its limitations by comparison with a high-precision, marker-based motion capture system, as a secondary contribution. SPiD has shown robustness by achieving this task using low-frequency and noisy perception. 4) *Generalization* aspect is validated by applying SPiD on the rope trajectory tracking task that has different cost function and goal. SPiD successfully generalized to this task, achieving high-speed trajectory following in simulation.

In summary, our main contributions are as follows:

- SPiD, the novel physics-informed self-supervised learning framework that consists of a physically accurate DLO model and the augmented self-supervised training strategy incorporating a DAgger variant. The framework is efficient, robust, and generalizable to new tasks and objects as demonstrated by the experiments.
- Extension of the mass-spring-based deformable object modeling by deriving damping terms that are proven valuable in dynamic motion prediction.

- Achieving the rope stabilization task by energy-based task formulation without expert demonstrations, with high data-efficiency, and robustness to perturbations and noisy observations. To demonstrate the generalization capability of our framework, we also address a dynamic rope endpoint trajectory tracking task.
- A data-driven markerless rope perception method for affordable and portable rope state estimation. Despite using low-cost hardware, the method achieves sufficient precision and update rate for real-time rope stabilization.

## II. RELATED WORK

This section reviews relevant work on modeling, manipulation and perception of deformable objects.

### A. Physical modeling

Previous studies on deformable object modeling have mainly relied on several mainstream physical formulations, including mass–spring systems (MSSs) [9], [17], [18], position-based dynamics (PBD) [19], [20], finite element methods (FEM) [21], and elastic rod models [22]. The MSSs has been widely adopted due to its high computational efficiency, but its accuracy is limited because of model simplifications [23]. PBD also provides fast simulation and good numerical stability, but focuses mainly on visual fidelity only [1]. FEM achieves high precision in modeling material deformation but requires significant computational resources, making it unsuitable for real-time applications. Elastic rod models are specifically designed for deformable linear object (DLO) modeling and provide a physically accurate description, but they similarly incur high computational costs. In this work, we adopt a mass–spring formulation augmented with derived damping terms to retain computational efficiency while capturing key dynamic effects.

### B. Data-driven modeling

Data-driven approaches aim to learn deformable object dynamics directly from sensory observations, often via neural transition models over particles, keypoints, or graphs. Beyond earlier purely data-driven pipelines such as ACID [5] and local-graph GNN models for deformable rearrangement [24], recent work has pushed toward higher-fidelity and more generalizable neural dynamics. For instance, Particle-Grid Neural Dynamics [4] leverages particle–grid representations to better capture complex deformation and contact; AdaptiGraph [25] learns graph-based neural dynamics conditioned on continuous physical property variables and adapts to unseen deformable objects via few-shot interaction. In addition, DeformNet [26] models deformable objects using PointNet with a recurrent state-space model to predict latent dynamics, which supports generalization to diverse simulated and real-world manipulation tasks.

These methods model complex nonlinear behaviors that are difficult to capture analytically. However, their performance heavily relies on the quantity and quality of training data, making them expensive to train in terms of both

data and computation. In contrast, our approach leverages a structured physical model with high data efficiency (using only 2,000 sampled data points in real-world experiments, as shown in Sec. V-A) and preserves physical interpretability.

### C. Quasi-static manipulation

Quasi-static manipulation assumes that deformable objects remain near force equilibrium during slow interactions, allowing inertial and dynamic effects to be neglected. This assumption has enabled a wide range of successful manipulation strategies by simplifying the underlying dynamics and reasoning primarily over object geometry. Representative works include global rope shape control [27], rope knotting [28], and cloth folding and smoothing [29].

Earlier approaches often relied on demonstration transfer or hand-designed geometric heuristics to generalize manipulation strategies to new configurations [30]. More recent works incorporate visual feedback, latent shape representations, or learning-based components to improve robustness and generalization under partial observability [1], [31]. These methods have demonstrated strong performance in tasks where object motion is slow and deformation evolves gradually. However, despite their effectiveness, quasi-static approaches infer the effects of actions primarily from object geometry, which often leads to slow and inefficient execution due to the need for iterative correction [2].

### D. Dynamic manipulation

Beyond quasi-static assumptions, dynamic manipulation explicitly considers inertial and transient effects during deformable object interaction, enabling faster and more agile behaviors. However, modeling and controlling deformable objects in dynamic regimes remains challenging due to complex, high-dimensional dynamics and limited observability.

Recent work has explored learning-based approaches to dynamic deformable manipulation. Using state diffusion and inverse dynamics models, Chen et al. [32] train policies capable of performing highly dynamic tasks such as laundry cleanup. Similarly, Lan et al. [33] propose the Dynamics-Informed Diffusion Policy, which integrates imitation pre-training with physics-informed test-time adaptation, and apply it to goal-conditioned dynamic rope manipulation. While these methods demonstrate strong performance, they rely on a large amount of expert demonstrations, which limits scalability to new tasks and objects. To reduce dependence on expert data, Lim et al. [34] propose collecting large-scale simulated trajectories using a simulator calibrated with limited real-world observations. However, this approach requires re-identification of physical parameters whenever the manipulated object changes, hindering robustness across objects with varying properties. In contrast, our method achieves data-efficient dynamic manipulation without expert demonstrations and generalizes robustly to deformable objects with diverse physical parameters.

### E. Rope perception

Despite extensive research on deformable object manipulation, robust rope perception in realistic and dynamic

environments remains an open problem [35]. Many existing methods rely on marker-based perception systems or assume static rope configurations and simplified geometric models, enabling accurate state estimation only under controlled conditions. Such approaches are difficult to deploy in unstructured settings. Vision-based methods also struggle with thin and elongated structures such as ropes due to frequent self-occlusions, rapidly changing shapes, and sensitivity to background clutter and illumination [36]. Recently, large pre-trained foundation models for segmentation have emerged as a promising alternative [37]; however, their performance degrades for highly deformable objects without task-specific fine-tuning, and their computational cost limits real-time applicability. Motivated by these limitations, we collect a task-specific dataset and fine-tune a lightweight, unified detection and segmentation model that enables accurate, real-time, markerless rope perception under dynamic conditions.

### III. SPiD: SELF-SUPERVISED PHYSICS-INFORMED DEFORMABLE OBJECT MANIPULATION

The SPiD framework consists of an offline phase and an online phase as illustrated in Fig. 2. The offline phase includes deformable linear object (DLO) modeling and system identification, as well as a self-supervised control learning module. The online phase deploys the learned neural policy for real-time control, while continuously performing out-of-distribution (OOD) detection, and uses a self-supervised DAgger mechanism to return to the control learning module to refine the controller and achieve more robust performance.

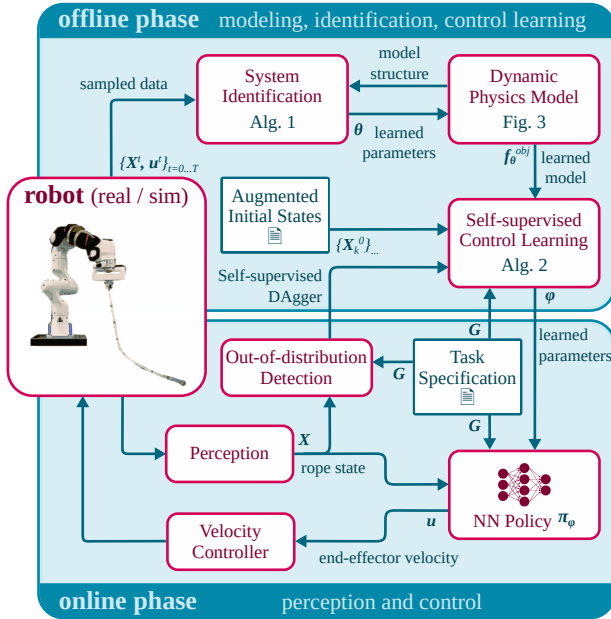


Fig. 2: The data flow of the SPiD framework.

In this section, we present the SPiD framework in three stages. First, we describe how we model a DLO in Sec. III-A and how its parameters are identified in Sec. III-B. Then, in Sec. III-C, we present the augmented self-supervised control learning algorithm together with the self-supervised DAgger mechanism.

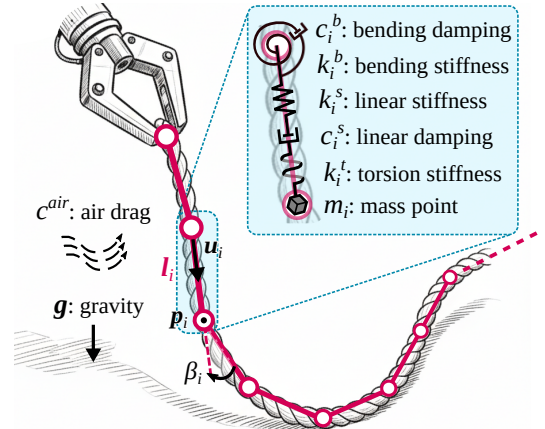


Fig. 3: The DLO model. The model consists of  $N+1$  mass points connected by linear springs/dampers, bending springs/dampers, and torsional springs. Additionally, air drag and gravity are incorporated into dynamics.

#### A. Modeling

As shown in Fig. 3, a DLO is modeled as a series of mass points connected by spring-damper elements. Each component—mass point, spring, and damper—is assigned independent parameters, providing the model with sufficient representational capacity to capture a wide range of physical properties, including those of heterogeneous ropes.

**Notation.** A DLO consists of  $N$  cable links ( $1, 2, \dots, N$ ) and  $N+1$  mass points ( $0, 1, \dots, N$ ). Each point has a mass  $m_i$ , and its state is denoted as  $\mathbf{x}_i = [\mathbf{p}_i^T, \mathbf{v}_i^T]^T$ , where  $\mathbf{p}_i \in \mathbb{R}^3$  and  $\mathbf{v}_i \in \mathbb{R}^3$  represent the position and velocity vectors, respectively. Therefore, the full state of the DLO has a dimension of  $6(N+1)$  and is represented as  $\mathbf{X} = [\mathbf{x}_0^T, \dots, \mathbf{x}_N^T]^T$ . The initial (rest) length of the  $i$ -th cable link is denoted as  $l_i^0$ . The current link vector is defined as  $\mathbf{l}_i = \mathbf{p}_i - \mathbf{p}_{i-1}$ , with its length  $l_i = \|\mathbf{l}_i\|$  and unit direction  $\mathbf{u}_i = \mathbf{l}_i / \|\mathbf{l}_i\|$ . The bending angle between two consecutive links  $\mathbf{l}_i$  and  $\mathbf{l}_{i+1}$  is expressed as  $\beta_i = \arccos(\mathbf{u}_i \cdot \mathbf{u}_{i+1})$ . Finally,  $\psi_i$  denotes the torsion angle of the  $i$ -th torsion spring.

**Linear spring-damper force** resists the change of distance and relative velocity between two connected mass points. Its expression on mass-point  $i$  is given by

$$\mathbf{F}_i^{\text{lin}} = -k_i^s(l_i - l_i^0)\mathbf{u}_i + k_{i+1}^s(l_{i+1} - l_{i+1}^0)\mathbf{u}_{i+1} - c_i^s((\mathbf{v}_i - \mathbf{v}_{i-1})^T \mathbf{u}_i)\mathbf{u}_i + c_{i+1}^s((\mathbf{v}_{i+1} - \mathbf{v}_i)^T \mathbf{u}_{i+1})\mathbf{u}_{i+1}, \quad (1)$$

where  $k_i^s$  and  $c_i^s$  denote the stiffness and damping coefficients of the  $i$ -th linear spring-damper element, respectively.

**Bending spring force** is an elastic restoring force generated when the bending angle (or curvature) between two adjacent links deviates from its reference value. Its expression on mass-point  $i$  is given by

$$\mathbf{F}_i^b = \frac{k_{i-1}^b \beta_{i-1}}{l_i} \frac{\mathbf{u}_i \times (\mathbf{u}_{i-1} \times \mathbf{u}_i)}{\sin \beta_{i-1}} - \frac{k_i^b \beta_i}{l_{i+1}} \frac{\mathbf{u}_{i+1} \times (\mathbf{u}_i \times \mathbf{u}_{i+1})}{\sin \beta_i} - \frac{k_i^b \beta_i}{l_i} \frac{\mathbf{u}_i \times (\mathbf{u}_i \times \mathbf{u}_{i+1})}{\sin \beta_i} + \frac{k_{i+1}^b \beta_{i+1}}{l_{i+1}} \frac{\mathbf{u}_{i+1} \times (\mathbf{u}_{i+1} \times \mathbf{u}_{i+2})}{\sin \beta_{i+1}}, \quad (2)$$

where  $k_i^b$  denotes the bending stiffness of the  $i$ -th bending spring [9]. The bending spring force can be decomposed into

two parts. In Eq. (2), the first and fourth terms correspond to the forces exerted on mass point  $i$  by its adjacent bending springs, while the middle two terms represent the reaction forces generated by the  $i$ -th bending spring itself.

**Bending damping force** exerts viscous resistance to the rate of change of bending deformation. During dynamic manipulation, where the deformation rate of the system is relatively high, the bending damping can have a non-negligible influence on the overall system dynamics. In Proposition 1, we derive the analytical formulation of the bending damping force.

**Proposition 1.** *Let  $c_i^b$  denote the bending damping coefficient of the  $i$ -th bending damper. The bending damping force acting on the  $i$ -th mass point is then given by*

$$\begin{aligned} \mathbf{F}_i^{\text{db}} &= \frac{c_{i-1}^b \dot{\beta}_{i-1}}{l_i} \frac{\mathbf{u}_{i-1} - \mathbf{u}_i \cos \beta_{i-1}}{\sin \beta_{i-1}} + \frac{c_i^b \dot{\beta}_i}{l_{i+1}} \frac{\mathbf{u}_{i+1} \cos \beta_i - \mathbf{u}_i}{\sin \beta_i} \\ &\quad - \frac{c_i^b \dot{\beta}_i}{l_i} \frac{\mathbf{u}_i \cos \beta_i - \mathbf{u}_{i+1}}{\sin \beta_i} + \frac{c_{i+1}^b \dot{\beta}_{i+1}}{l_{i+1}} \frac{\mathbf{u}_{i+1} \cos \beta_{i+1} - \mathbf{u}_{i+2}}{\sin \beta_{i+1}}, \end{aligned} \quad (3)$$

where  $\dot{\beta}_i$  represents the rate of change of the bending angle, obtained as

$$\dot{\beta}_i = \frac{\mathbf{v}_i - \mathbf{v}_{i-1}}{l_i} \frac{\mathbf{u}_i \cos \beta_i - \mathbf{u}_{i+1}}{\sin \beta_i} + \frac{\mathbf{v}_{i+1} - \mathbf{v}_i}{l_{i+1}} \frac{\mathbf{u}_{i+1} \cos \beta_i - \mathbf{u}_i}{\sin \beta_i}. \quad (4)$$

*Proof.* The partial derivative of the bending angle  $\beta_i$  with respect to the link vector  $\mathbf{l}_i$  can be expressed as

$$\begin{aligned} \frac{\partial \beta_i}{\partial \mathbf{l}_i} &= \frac{d(\arccos(\cos \beta_i))}{d(\cos \beta_i)} \frac{\partial}{\partial \mathbf{l}_i} \left( \frac{\mathbf{l}_i \cdot \mathbf{l}_{i+1}}{\|\mathbf{l}_i\| \|\mathbf{l}_{i+1}\|} \right) \\ &= -\frac{1}{\sin \beta_i} \frac{\|\mathbf{l}_i\|^2 \mathbf{l}_{i+1} - (\mathbf{l}_i \cdot \mathbf{l}_{i+1}) \mathbf{l}_i}{\|\mathbf{l}_i\|^3 \|\mathbf{l}_{i+1}\|} = \frac{\mathbf{u}_i \cos \beta_i - \mathbf{u}_{i+1}}{\sin \beta_i \|\mathbf{l}_i\|}. \end{aligned} \quad (5)$$

Similarly, the derivative of  $\beta_i$  with respect to the adjacent link  $\mathbf{l}_{i+1}$  is given by

$$\frac{\partial \beta_i}{\partial \mathbf{l}_{i+1}} = \frac{\mathbf{u}_{i+1} \cos \beta_i - \mathbf{u}_i}{\sin \beta_i \|\mathbf{l}_{i+1}\|}. \quad (6)$$

By applying the chain rule, the derivatives of  $\beta_i$  with respect to the three connected mass points  $\mathbf{p}_{i-1}$ ,  $\mathbf{p}_i$ , and  $\mathbf{p}_{i+1}$  satisfy the following relations:

$$\frac{\partial \beta_i}{\partial \mathbf{p}_{i-1}} = -\frac{\partial \beta_i}{\partial \mathbf{l}_i}, \quad \frac{\partial \beta_i}{\partial \mathbf{p}_i} = \frac{\partial \beta_i}{\partial \mathbf{l}_i} - \frac{\partial \beta_i}{\partial \mathbf{l}_{i+1}}, \quad \frac{\partial \beta_i}{\partial \mathbf{p}_{i+1}} = \frac{\partial \beta_i}{\partial \mathbf{l}_{i+1}}. \quad (7)$$

Consequently, the time derivative of the bending angle  $\beta_i$  can be written in terms of the velocities of the three adjacent mass points:

$$\dot{\beta}_i = \frac{\partial \beta_i}{\partial \mathbf{p}_{i-1}} \cdot \mathbf{v}_{i-1} + \frac{\partial \beta_i}{\partial \mathbf{p}_i} \cdot \mathbf{v}_i + \frac{\partial \beta_i}{\partial \mathbf{p}_{i+1}} \cdot \mathbf{v}_{i+1}. \quad (8)$$

Substituting Eqs. (5) to (7) into Eq. (8) and rearranging yields Eq. (4). According to the principle of virtual work,  $\delta W = -c_i^b \dot{\beta}_i \delta \beta_i = \sum_k \mathbf{F}_{i \rightarrow k}^{\text{db}} \cdot \delta \mathbf{p}_k$ , where  $\mathbf{F}_{i \rightarrow k}^{\text{db}}$  denotes the force exerted by the  $i$ -th bending damper on  $k$ -th mass point, which can be expressed as

$$\mathbf{F}_{i \rightarrow k}^{\text{db}} = -c_i^b \dot{\beta}_i \frac{\partial \beta_i}{\partial \mathbf{p}_k}, \quad k \in \{i-1, i, i+1\}. \quad (9)$$

Finally, the total bending damping force acting on the  $i$ -th mass point is obtained by summing the contributions from the three neighboring bending dampers ( $i-1, i, i+1$ ):

$$\mathbf{F}_i^{\text{db}} = \mathbf{F}_{i-1 \rightarrow i}^{\text{db}} - \mathbf{F}_{i \rightarrow i-1}^{\text{db}} - \mathbf{F}_{i \rightarrow i+1}^{\text{db}} + \mathbf{F}_{i+1 \rightarrow i}^{\text{db}}.$$

By substituting Eqs. (5) to (7) and (9) into the above expression and simplifying, we obtain Eq. (3).  $\square$

**Torsion spring force** consists of two components: material torsion and geometric torsion. Material torsion originates from the internal shear stress induced by twisting along the rope's longitudinal axis, representing the material's elastic resistance to angular deformation [38], [39]. In a rope manipulation task, the free end allows this torsional energy to dissipate quickly through rotation, rendering the material torsion negligible. Hence, the torsion angle  $\psi_i$  is the geometric torsion angle in our model.

Each cable link  $\mathbf{l}_i$  together with its adjacent links  $\mathbf{l}_{i-1}$  and  $\mathbf{l}_{i+1}$  forms two planes, and the angle between these planes defines the geometric torsion angle  $\psi_i$ . By taking the partial derivative of the torsional potential energy with respect to the position of mass point  $i$ , the torsion spring force acting on this point can be obtained [9] as

$$\mathbf{F}_i^t = -\frac{\partial E^t}{\partial \mathbf{x}_i}, \quad E^t = \frac{1}{2} \sum_{j=1}^N k_j^t \psi_j^2, \quad (10)$$

where  $k_j^t$  denotes the torsional stiffness of the  $j$ -th torsion spring.

**External forces** in our model consist of gravity and air resistance. The total external force acting on the  $i$ -th mass point is expressed as

$$\mathbf{F}_i^{\text{ext}} = m_i \mathbf{g} - c^{\text{air}} \mathbf{v}_i, \quad (11)$$

where  $\mathbf{g}$  denotes the gravitational acceleration vector, and  $c^{\text{air}}$  is the air damping coefficient.

**Forward time integration** refers to the numerical process of advancing the system states over time by discretizing the given equations of motion. By combining Eqs. (1) to (4), (10) and (11) with Newton's second law, the equations of motion for each mass point are obtained

$$\mathbf{a}_i = \left( \mathbf{F}_i^{\text{lin}} + \mathbf{F}_i^{\text{b}} + \mathbf{F}_i^t + \mathbf{F}_i^{\text{db}} + \mathbf{F}_i^{\text{ext}} \right) / m_i, \quad (12)$$

which is then integrated forward in time using the *symplectic Euler* scheme

$$\begin{aligned} \mathbf{v}_i^{t+1} &= \mathbf{v}_i^t + \Delta t \mathbf{a}_i^t, \\ \mathbf{x}_i^{t+1} &= \mathbf{x}_i^t + \Delta t \mathbf{v}_i^{t+1}, \end{aligned} \quad (13)$$

where  $\Delta t$  denotes the integration time step, and the superscript  $t$  indicates the current time step.

**Incorporating control input.** So far, the DLO has been modeled as a discrete autonomous system. To obtain a fully controlled DLO model, we now introduce the control input  $\mathbf{u}$ . The top end of the DLO is attached to the end-effector of a manipulator, which in our experiments is driven by a Cartesian-space velocity controller. This low-level controller is capable of accurately tracking smooth and physically feasible velocity commands, and for lightweight objects like

ropes, the reaction force generated by its swinging on the manipulator can be neglected. Therefore, it is reasonable to assume that the commanded end-effector velocity  $\mathbf{u}$  directly determines the velocity of the first mass point of the DLO:

$$\mathbf{v}_0 = \mathbf{u} \text{ (control input).} \quad (14)$$

Under this constraint, the acceleration of the first mass point  $\mathbf{a}_0$  becomes redundant and does not participate in the system evolution. Combining condition (14) with Eqs. (12) and (13), we obtain the discrete controlled DLO dynamics as

$$\mathbf{X}^{t+1} = \mathbf{f}_{\theta, \Delta t}^{\text{dlo}}(\mathbf{X}^t, \mathbf{u}^t), \quad (15)$$

where  $\theta$  denotes all the to-be-identified model parameters (e.g.,  $k_i^s$ ,  $c_i^s$ ,  $k_i^b$ , etc) and  $\mathbf{X}$  denotes full DLO state  $\mathbf{X} = [\mathbf{x}_0^T, \dots, \mathbf{x}_N^T]^T$ .

### B. System identification

After deriving the mathematical model of the controlled system, the model parameters  $\theta$  are identified to obtain a high-fidelity dynamic model that accurately captures the real system dynamics. Specifically,  $\theta$  consists of the particle mass vector  $\mathbf{m} = \{m_i\}_{i=0}^N$ , the initial link-length vector  $\mathbf{l}^0 = \{l_i^0\}_{i=1}^N$ , the gravitational acceleration vector  $\mathbf{g}$ , the aerodynamic drag coefficient  $c^{air}$ , and the rope stiffness and damping parameters, including the linear spring and damping vectors  $\mathbf{k}^s = \{k_i^s\}_{i=1}^N$  and  $\mathbf{c}^s = \{c_i^s\}_{i=1}^N$ , the bending spring and damping vectors  $\mathbf{k}^b = \{k_i^b\}_{i=1}^{N-1}$  and  $\mathbf{c}^b = \{c_i^b\}_{i=1}^{N-1}$ , as well as the torsional stiffness vector  $\mathbf{k}' = \{k_i'\}_{i=2}^{N-1}$ , as illustrated on Fig. 3. In compact form, we denote the full parameter set as

$$\theta = \{\mathbf{m}, \mathbf{l}^0, \mathbf{g}, c^{air}, \mathbf{k}^s, \mathbf{c}^s, \mathbf{k}^b, \mathbf{c}^b, \mathbf{k}'\}.$$

Among these parameters,  $\mathbf{m}$  and  $\mathbf{l}^0$  can be obtained via direct measurement,  $\mathbf{g}$  is known from physics, and the remaining parameters are estimated through system identification.

Since the model in Eq. (15) is differentiable, a differentiable physics-based system identification approach is adopted as shown in Algorithm 1, where the symbol  $\hat{\cdot}$  denotes predicted variables. For convenience, we denote the positions of all rope nodes as  $\mathbf{P} = [\mathbf{p}_0^T, \dots, \mathbf{p}_N^T]^T$  and the velocities as  $\mathbf{V} = [\mathbf{v}_0^T, \dots, \mathbf{v}_N^T]^T$ , which are contained in  $\mathbf{X}$ . The core idea is to initialize the reference system and our model with the same initial state, excite them with identical inputs, quantify the discrepancy between their resulting state trajectories as the loss function, and update the model parameters via gradient-based optimization, so that the simulated dynamics progressively converge to those of the real system. However, in the real system the motion-capture perception system only provides position measurements rather than velocities. Therefore, only the position (measurable) part of the state trajectory is used for comparison. The rope remains stationary until the initial release, implying zero initial velocity. Together with the initial position provided by the motion-capture system, the complete initial state of the rope is therefore available.

In the simulation experiments, the rope consists of 21 mass points, resulting in nearly one hundred parameters to be identified. When processing long time-series data with

---

### Algorithm 1 Differentiable Physics System Identification

**Input:** Dataset  $\{(\mathbf{P}^t, \mathbf{u}^t)\}_{t=0 \dots T}$ , initial horizon  $H$ , horizon increment  $\Delta H$ , sampling interval  $h$ , integration time step  $\Delta t$ , loss threshold  $\varepsilon$   
**Output:** Identified model parameters  $\theta$

- 1: Initialize parameters  $\theta$ ,  $\hat{\mathbf{P}}^0 = \mathbf{P}^0$ ,  $\hat{\mathbf{V}}^0 = \mathbf{0}$
- 2: Obtain  $\hat{\mathbf{X}}^0$  by combining  $\hat{\mathbf{P}}^0$  and  $\hat{\mathbf{V}}^0$ ; set  $\hat{\mathbf{X}}' \leftarrow \hat{\mathbf{X}}^0$
- 3: **while**  $H \leq T$  **do**
- 4:   **for**  $t = 0, \dots, H$  **do**
- 5:     **iterate**  $\hat{\mathbf{X}}' \leftarrow \mathbf{f}_{\theta, \Delta t}^{\text{dlo}}(\hat{\mathbf{X}}', \mathbf{u}^t)$  **for**  $h/\Delta t$  **steps**
- 6:      $\hat{\mathbf{X}}'^{t+1} \leftarrow \hat{\mathbf{X}}'$   $\triangleright \hat{\mathbf{X}}'^{t+1}$  includes  $\hat{\mathbf{P}}^{t+1}$
- 7:   **end for**
- 8:    $\mathbf{L}_p \leftarrow \frac{1}{H} \sum_{t=1}^H \|\hat{\mathbf{P}}^t - \mathbf{P}^t\|_2^2$
- 9:   Update  $\theta \leftarrow \text{Adam}(\theta, \nabla_{\theta} \mathbf{L}_p)$   $\triangleright$  Autodiff
- 10:   **if**  $\mathbf{L}_p < \varepsilon$  **then**
- 11:      $H \leftarrow H + \Delta H$
- 12:   **end if**
- 13: **end while**

---

such a large number of parameters, the increased recurrence depth (Alg. 1, lines 4–8) amplifies the parameter-to-loss nonlinearity, leading to a highly non-convex loss landscape and causing the optimization to be frequently trapped in suboptimal local minima. To address this issue, two curriculum-learning strategies are introduced. The first one is a variable-horizon strategy (Alg. 1: line 11), where a relatively short horizon  $H$  is used at the beginning, and  $H$  is gradually increased once the loss falls below a predefined threshold, until it eventually reaches the full data length  $T$ . The second one is a two-stage parameter strategy. In the first identification stage, all springs and dampers of the same type are constrained to share a common parameter across the rope, so that the rope is treated as a homogeneous system. After this stage converges, the identified parameters are used as initialization, and the constraint is relaxed so that each spring and damping parameter is treated independently, forming a heterogeneous rope model for a refined identification stage. These two curriculum-learning strategies significantly improve optimization stability and help the model converge toward the true system parameters.

Finally, since the sampling interval  $h$  and the integration time step  $\Delta t$  of the model may differ, an additional procedure is required to ensure temporal alignment of the trajectories (Alg. 1: line 5). In the real-world experiment, the motion-capture system provides measurements at a sampling interval of 10 ms, whereas the integration time step of our model is 1 ms. Therefore, line 5 needs to be iterated 10 times to propagate the model to the next measurement instant.

### C. Augmented self-supervised neural controller learning

After obtaining an accurate physical model, we are able to train a task-oriented controller based on it. At this phase, we train a neural network to learn behaviors that minimize a given task-oriented loss function  $\mathbf{L}_{\text{task}}(\cdot)$ . The controller  $\pi_{\phi}(\cdot)$  takes as input the current rope state  $\mathbf{X} = [\mathbf{x}_0^T, \dots, \mathbf{x}_N^T]^T$

**Algorithm 2** Physics-informed Self-supervised Training

---

**Input:** Initial state set  $\{\mathbf{X}_k^0\}_{k=1,\dots,K}$ , task specification set  $\{\mathbf{G}_k\}_{k=1,\dots,K}$ , model parameters  $\theta$ , integration time step  $\Delta t$   
**Output:** Trained controller parameters  $\phi$

- 1: Initialize controller parameters  $\phi$
- 2: **for** each training iteration **do**
- 3:      $\{\Delta\theta_k\}_{k=1,\dots,K} \leftarrow \text{sample\_noise}(\theta)$
- 4:     **for**  $t = 0, \dots, T-1$  **do**
- 5:          $\{\mathbf{u}_k^t\}_{k=1,\dots,K} \leftarrow \{\pi_\phi(\mathbf{X}_k^t, \mathbf{G}_k)\}_{k=1,\dots,K}$
- 6:          $\{\mathbf{X}_k^{t+1}\}_{k=1,\dots,K} \leftarrow \{f_{\theta+\Delta\theta_k, \Delta t}^{\text{dlo}}(\mathbf{X}_k^t, \mathbf{u}_k^t)\}_{k=1,\dots,K}$
- 7:     **end for**
- 8:      $\mathbf{L} \leftarrow \frac{1}{K} \sum_{k=1}^K \mathbf{L}_{\text{task}}(\{\mathbf{X}_k^t\}_{t=1}^T, \mathbf{G}_k)$   
▷ Task-based  $\mathbf{L}_{\text{task}}(\cdot)$  as in (18) and (19)
- 9:      $\phi \leftarrow \text{Adam}(\phi, \nabla_\phi \mathbf{L})$   
▷ Autodiff
- 10: **end for**

---

together with the task specification  $\mathbf{G}$ , and outputs a 3-D velocity command  $\mathbf{u}$  for the robot end-effector in Cartesian space. The specific designs of  $\mathbf{L}_{\text{task}}(\cdot)$  and  $\mathbf{G}$  for the rope stabilization and trajectory tracking tasks will be presented in Sec. V.

The self-supervised learning process is summarized in Algorithm 2. In each training iteration, a batch of  $K$  rollouts is executed in parallel. In each training rollout, the controller interacts with the rope model for  $T$  simulation steps, producing a state trajectory  $\{\mathbf{X}_k^t\}_{t=1}^T$ . This trajectory, together with the task specification  $\mathbf{G}_k$ , is then fed into the loss function  $\mathbf{L}(\cdot)$  to compute the batch loss. Finally, the gradients are computed via backpropagation and used to update the controller parameters. To enhance robustness and generalization, our framework incorporates several augmentation strategies during training. Specifically, we propose four key operations to achieve this goal:

**Initial state diversity:** To enable the controller to handle diverse configurations, we ensure that the initial state set  $\{\mathbf{X}_k^0\}_{k=1,\dots,K}$  is sufficiently diverse, so that rope states encountered in practice can be viewed as interpolations within this set. To construct such diversity, we apply random motions to the rope and record its states at different time steps. Meanwhile, the data collected during system identification is also included in the initial state set. In the experiment phase, around  $10k$  states were collected with this method. However, even with these samples, the collected states only cover a few sparse trajectories in the 3D physical space; thus, additional data augmentation is required.

**Data augmentation:** All the recorded rope states are first translated so that their top endpoints coincide at a common point. Then, we uniformly rotate each rope around the  $z$ -axis by small angular increments, covering  $360^\circ$ . Lastly, the replicated data are duplicated along the  $x$ ,  $y$ , and  $z$  directions with equal spacing. In total,  $\sim 2$  million states are generated after this augmentation in the experiment. Through these spatial rotations and translations, the resulting dataset achieves comprehensive coverage of the 3D physical space.

**Self-supervised DAgger:** We extend the core idea of DAgger [40] to a self-supervised learning setting, enabling automatic detection and correction of distribution shifts with-

out requiring expert labels. Since the controller is trained to minimize the loss associated with the resulting state trajectory, a well-trained controller should, during deployment, continuously decrease the loss or maintain it at a low level, which corresponds to successful task execution. Therefore, in practice, we monitor the loss evolution online. When the loss fails to decrease, exhibits abnormal growth over a period of time, or even diverges, the corresponding states are identified as out-of-distribution (OOD) samples. These OOD samples, together with their corresponding task specifications, are then added back into the initial-state and task-specification sets with higher sampling weights for further offline policy refinement.

Specifically, in the rope stabilization task, the rope energy is used as the loss, and the controller is expected to continuously dissipate this energy until it approaches zero, which corresponds to the rope coming to rest. During deployment, we compute the rope energy in real time; if the energy abnormally increases or oscillates around a positive value, we regard this as an OOD event and record the corresponding state. In the trajectory-tracking task, the controller is expected to continuously drive the rope tip to follow a moving target; therefore, the loss is defined as the deviation between the rope-tip trajectory and the target trajectory. During deployment, we monitor the real-time distance between the rope tip and the target; when this distance exceeds a predefined threshold, an OOD event is triggered, and both the current rope state and the associated trajectory segment are recorded. This automatic detection and correction mechanism enables the controller to progressively compensate for deficiencies in the training data and ultimately achieve robust and reliable performance without requiring expert demonstrations.

**Domain randomization:** During training, additional noise is injected into the rope model to enhance the controller's robustness and generalization across ropes with different physical properties. In each iteration, we sample  $K$  Gaussian noise vectors  $\Delta\theta_k$  and add them to the original model parameters to simulate ropes with varying characteristics (Alg. 2: line 3 and 6). Experimental results show that the controller trained with this strategy can effectively handle ropes with diverse physical attributes.

#### IV. ROPE PERCEPTION

Estimating the rope states constitutes a challenging perception problem as ropes are thin and lightweight objects that are hard to distinguish visually, especially when they move fast. High frequency and high accuracy perception is vital for achieving agile manipulation. Thus, we primarily used high-performance marker-based perception to evaluate the control performance of SPiD and the baseline. However, marker-based systems are not feasible in many application scenarios. For this reason we also developed a markerless perception system to validate the application of our method in a more affordable single camera setup. Despite the physical limitations of the markerless system, our experiments

show successful rope stabilization in Sec. V-C. We detail both perception approaches below.

### A. Marker-based perception

We use off-the-shelf OptiTrack motion capture system as our default perception method. It requires multiple infrared cameras and reflective markers on the objects to track and reconstruct the 3D positions of the markers. For rope tracking, a series of equally distanced markers are attached on the rope. The resulting measurements provide high-precision and high-rate state feedback as an external perception module. Specifics of our setup are presented in Sec. V-B.4.

### B. Markerless perception

We propose a markerless, vision-based pipeline for rope detection and segmentation using a single RGB camera, enabling robust rope perception in realistic manipulation scenarios without reliance on external motion capture systems or artificial markers. To this end, we design and evaluate a deep learning-based segmentation pipeline, exploring multiple architectural and implementation choices and refining the system to satisfy both real-time performance and segmentation accuracy requirements.

1) *Rope detection and segmentation*: The backbone of our markerless perception approach is the detection and segmentation of the rope from RGB images. To this end, we investigated several relevant pretrained models, including Grounding Dino [41] for rope detection which is a powerful, zero-shot object detection model that allows to find and draw bounding boxes around any object in an image by using a text prompt. For segmentation, we choose Segment Anything Model (SAM) [37], which is known to perform well on generic objects, and Mobile-SAM [42], a lightweight variant designed for faster inference. In addition, we collected a dedicated rope RGB dataset and fine-tuned YOLOv11-seg (medium size) [43], a unified model for rope detection and segmentation that directly predicts instance-level segmentation masks. We compared these segmentation approaches in terms of computational cost and prediction performance and ultimately selected our fine-tuned YOLOv11-seg model, as it provides the best accuracy and inference time. Detailed comparisons and implementation details are presented in Sec. V-C.

To tailor the segmentation model to the rope perception task, we collected a dedicated rope RGB dataset, in which images were annotated with instance-level segmentation masks. The data collection and annotation procedures are detailed in Sec. V-C.1. Based on this dataset and its annotations, we fine-tuned a YOLOv11-seg model, which jointly performs object detection and instance segmentation in a single forward pass. The model directly predicts bounding boxes, class confidences, and pixel-wise segmentation masks for the rope class. Post-processing applies confidence thresholding to remove unreliable detections, after which all valid instances are merged to form a consolidated rope segmentation.

2) *Rope splitter algorithm*: For precise and high-fidelity manipulation of a rope, we split the rope into equidistant points as illustrated in Fig. 3, and include their positions and velocities in the rope state  $\mathbf{X}$  (Sec. III-A). We developed an algorithm to achieve consistent and computationally efficient rope splitting for a given segmentation mask. We preprocess the mask using the *skeletonize* procedure<sup>1</sup> to reduce it into the central points  $\mathbf{P}_m = \{\mathbf{p}_{m,j} \in \mathbb{R}^2 | j = 0 \dots M\}$ . The algorithm iteratively processes these points to identify  $N$  split points  $\mathbf{p}_{s,i}$ , starting from the initial mask point ( $\mathbf{p}_{s,0} = \mathbf{p}_{m,0}$ ). For each split point  $\mathbf{p}_{s,i}$ , the next split point  $\mathbf{p}_{s,i+1}$  is identified as the closest point whose distance  $d_{i,j}$  ( $\|\mathbf{p}_{m,j} - \mathbf{p}_{s,i}\|$ ) is greater than a predefined splitting distance  $d_{\min}$ , and less than the distance to the previous splitting point  $\mathbf{p}_{s,i-1}$  to avoid going backwards:

$$\mathbf{p}_{s,i+1} \leftarrow \arg \min_{\mathbf{p}_{m,j} \in \mathbf{P}_m} d_{i,j} \quad \text{s.t.} \quad d_{i,j} \geq d_{\min}, \quad d_{i,j} < \|\mathbf{p}_{m,j} - \mathbf{p}_{s,i-1}\|. \quad (16)$$

The main bottleneck of this algorithm is finding the closest candidate points to the current split point  $\mathbf{p}_{s,i}$ , which has  $\mathcal{O}(M^2)$  brute force complexity. For efficiency, we sort the points into a *KD tree* structure at each frame, which is used to efficiently query the closest points to a given point. In our preliminary tests, this choice reduced the rope splitting time from 1092 ms (brute force) to 15 ms (KD tree) for a segmentation mask of 3300 pixels.

Please note that this approach ignores the curvature between each split point, causing drift when the curvature is high. We alleviate this issue by segmenting at a higher fidelity first (e.g.,  $cN$  splits), and selecting  $N$  equally distanced final points among them.

## V. EXPERIMENTS AND RESULTS

We evaluate our contributions in four sections. Section V-A presents the model validation experiment that measures the effect of the novel modeling terms. Section V-B consists of our core experiments, showing the performance of the proposed controller in an agile rope manipulation task, under changing object configurations and external perturbations. In Section V-C, the rope perception approach is replaced with the more affordable but low-fidelity markerless perception. SPiD achieves effective rope stabilization also in this condition. Section V-D demonstrates the generalization capacity of SPiD by applying it on the rope trajectory tracking task, which is distinct from rope stabilization.

### A. Model validation

Compared to the previous mass–spring model [9], we incorporate damping components to better capture the dynamic characteristics of the rope. To verify the higher fidelity of *our model*, the previous method is used as the *baseline model* [9] for comparison. We validate the proposed approach both in simulation using the MuJoCo platform and in real-world

<sup>1</sup>scikit-image.org

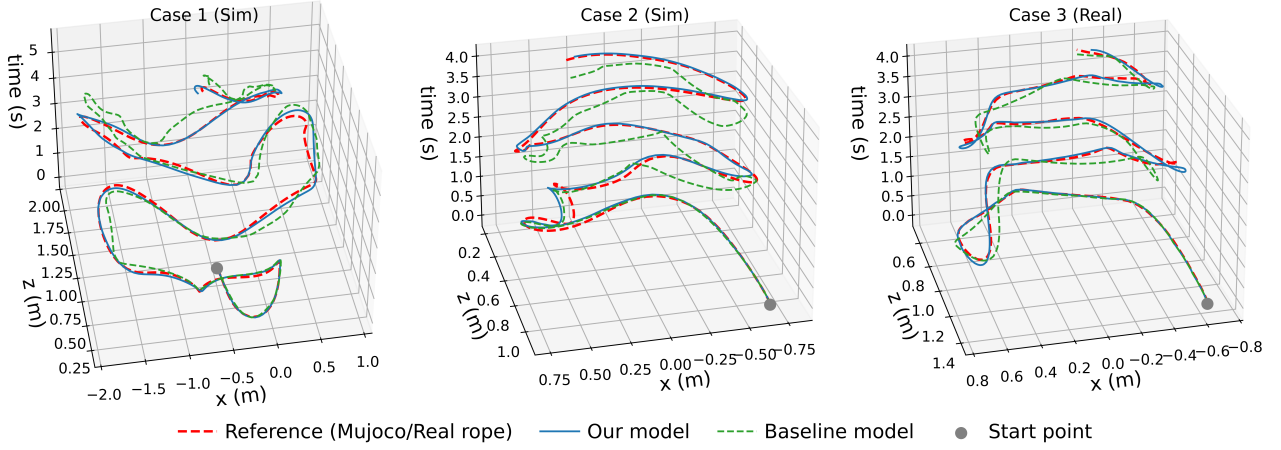


Fig. 4: **Model validation.** Rope tip trajectories of the reference rope (Mujoco or real), *our model*, and the *baseline model* under three unseen initial states. Our model can predict future states with higher accuracy than the baseline model.

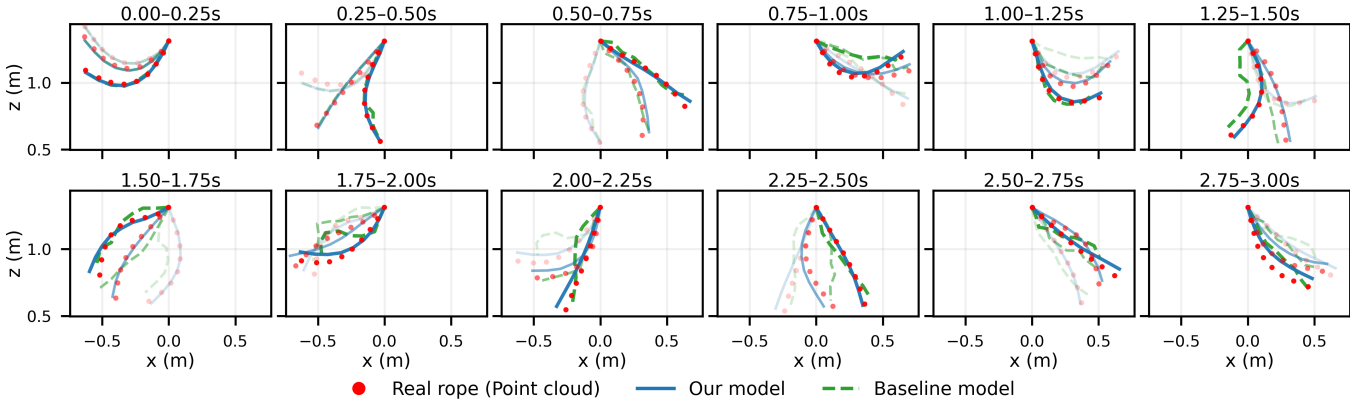


Fig. 5: **Rope's motion sequence of Case 3 (Real).** The motion trajectory of the rope over the first 3 s after release. Each subplot corresponds to a 0.25 s time window and shows three uniformly sampled rope configurations. Lighter colors indicate earlier time instances.

TABLE I: RMSE of the rope tip position prediction in three experiment cases.

Model \ Case	Case 1 (Sim)	Case 2 (Sim)	Case 3 (Real)
Baseline model	0.1510	0.1347	0.0810
Our model	<b>0.0704</b>	<b>0.0442</b>	<b>0.0591</b>

experiments. Accordingly, two rope models are identified using Alg. 1: One for simulation and one for the real world. During training, both the *baseline model* and *our model* are trained on identical datasets, using 5,000 state-action samples in simulation and 2,000 samples in the real-world experiment, demonstrating high data efficiency. During evaluation, two unseen initial states are tested in the MuJoCo simulation, and one unseen initial state is tested in the real-world experiment. The RMSE between the rope tip position and the reference rope tip position is used as a quantitative metric to assess model accuracy.

The identification results are shown in Fig. 4, where each curve represents the trajectory of the corresponding rope tip. All three models start from identical unseen initial states and then evolve solely according to their own system dynamics.

For clarity of visualization, the rope motion is constrained to mainly lie in the  $x-z$  plane, while the displacement along the  $y$ -axis is relatively small and therefore neglected. As a result, Fig. 4 illustrates only the rope tip  $x-z$  trajectories over time.

In the MuJoCo simulation experiments, the first case adopts a relatively small initial bending angle, and the top end of the rope is moved within the  $x-z$  plane over a total duration of 5.5s. In contrast, the second case uses a larger initial bending angle, while the top end of the rope is fixed for 4s. As shown in Case 1 and Case 2 of Fig. 4, our model demonstrates more accurate modeling performance. Specifically, our model closely tracks the ground truth throughout the entire experiment, whereas the baseline model matches the ground truth for only approximately 3.5s in the first case and approximately 1.5s in the second case. Similar trends are reflected in Table I, where our model achieves significantly lower RMSE values compared to the baseline model.

In the real-world experiment, a large initial bending angle is applied to the rope. After release, the top end of the rope is kept fixed, allowing the rope to swing freely. Case 3 in Fig. 4 shows the rope tip trajectories over the first 4s. To

better illustrate the modeling performance, Fig. 5 presents the complete rope motion over the first 3s in Case 3. Red points denote the real rope node point cloud obtained from the OptiTrack system, the blue curve represents the rope motion predicted by our model, and the green dashed curve represents that predicted by the baseline model. As can be observed, during the initial 0.75s, both our model and the baseline model accurately reproduce the real rope motion. However, in the 0.75–1.0s interval, the baseline model begins to exhibit noticeable errors in the rope configuration. After this point, although it remains consistent with the real rope in terms of the overall swinging trend, significant distortions appear in the detailed rope shape. In contrast, our model is able to accurately capture the evolution of the rope shape throughout the entire process. This observation is further supported by Table I, which shows that our model achieves higher accuracy than the baseline model in Case 3.

### B. Rope stabilization

We use the rope stabilization task as our primary testbed for evaluating our neural controller's agile manipulation performance. This task requires fast responses to the highly dynamic and nonlinear rope motions.

We demonstrate the performance of the proposed controller through simulation and real-world experiments. In each of simulation and real-world settings, a single neural controller is trained. Then, it is tested across different rope types and initial positions to demonstrate its effectiveness and generalization capability.

In this task, we do not use task specification ( $\mathbf{G} = \emptyset$ ) and use an energy-based loss for self-supervised control learning as detailed below.

#### 1) Task formulation:

**Loss function.** We use the total energy of the system to quantify the degree of rope swing. Accordingly, the controller is trained to perform maximum negative work at each step, thereby stabilizing the rope as soon as possible. The rope energy consists of the gravitational potential and kinetic energies of all mass points, as well as the elastic potential energy stored in the springs:

$$E_{\text{rope}}(\mathbf{X}) = \sum_{i=0}^N (m_i g z_i + \frac{1}{2} m_i \|\mathbf{v}_i\|^2) + \frac{1}{2} \sum_{i=1}^{N-1} k_i^b \beta_i^2 + \frac{1}{2} \sum_{i=1}^N k_i^s (l_i - l_i^0)^2 + \frac{1}{2} \sum_{i=1}^N k_i^t \psi_i^2, \quad (17)$$

where  $\mathbf{X}$  denotes the full state of the rope, and  $z_i$  represents the third (vertical) component of the position vector  $\mathbf{p}_i$ . In this task, the vertical component of the velocity command  $\mathbf{u}$  is fixed to zero, as the loss function  $E_{\text{rope}}(\cdot)$  accounts for gravitational potential energy; otherwise, the controller would continuously move the end-effector downward to minimize total energy.

During training, we only consider the rope energy at the final time step. Therefore, given a state trajectory  $\{\mathbf{X}^t\}_{t=1}^T$ , the training loss is defined as the rope energy at the terminal state:

$$L_{\text{task}}(\{\mathbf{X}^t\}_{t=1}^T, \mathbf{G} = \emptyset) = E_{\text{rope}}(\mathbf{X}^T). \quad (18)$$

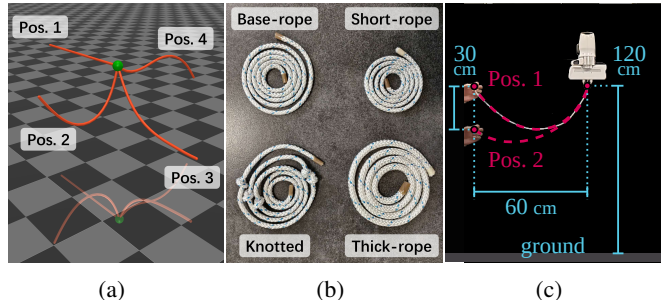


Fig. 6: **Test cases.** (a) Four unseen initial rope positions are used in simulation. (b) Four ropes with different masses, lengths and non-uniform mass distributions are used in the real world. (c) Two initial rope positions are used in the real world.

**Metrics.** We continue to use the energy  $E_{\text{rope}}(\cdot)$  defined in Eq. (17) to measure the swinging motion of the rope in the evaluation. The rope is considered stabilized when its energy decreases to 1% of the initial value.

2) *Baseline controller:* To validate the effectiveness of our proposed controller, we implement the baseline from [10]. This baseline was originally developed for anti-swing control in a crane system, where the load is stabilized by controlling the motion of the cable's top end. The method models the cable as a double pendulum and proves the stability of the corresponding control law. In the original work, the control was applied only along the  $x$ -axis, while in our implementation, it has been extended to the  $x$ - $y$  plane.

#### 3) Simulation experiments:

**Setup.** The simulation experiments are conducted in MuJoCo 3.2.2 using a 1m rope model composed of 40 serially connected rigid segments. We manipulate the rope by controlling the velocity of its top end in the  $x$ - $y$  plane at 100Hz. Through the Python interface, the position and velocity of each segment's base can be accessed. We evaluate the generalization capability of the proposed algorithm on four different initial rope positions (Fig. 6a). For each initial position, we test the methods on  $5^3$  rope models with parameters uniformly sampled for the twist modulus in  $[0, 1 \times 10^7]$  Pa, bending modulus in  $[0, 1 \times 10^7]$  Pa, and segment mass in  $[1.5, 3.5]$  g.

**Results.** The simulation results are shown in Fig. 7. The four subfigures correspond to the four initial positions illustrated in Fig. 6a. In each subfigure, the blue, orange, and green curves represent the energy evolution of the rope under our controller (Sec. III-C), the baseline method (Sec. V-B.2), and the passive condition, respectively. The passive case means that the top end of the rope remains fixed, and the energy decays naturally through air drag and internal damping. Each curve shows the average energy trajectory over  $5^3$  different rope parameter settings. It can be observed that our controller achieves the fastest and smoothest performance in all cases, while the baseline controller takes longer and exhibits noticeable oscillations.

#### 4) Real-world experiments:

**Setup.** In real-world experiments, we use a Franka Emika

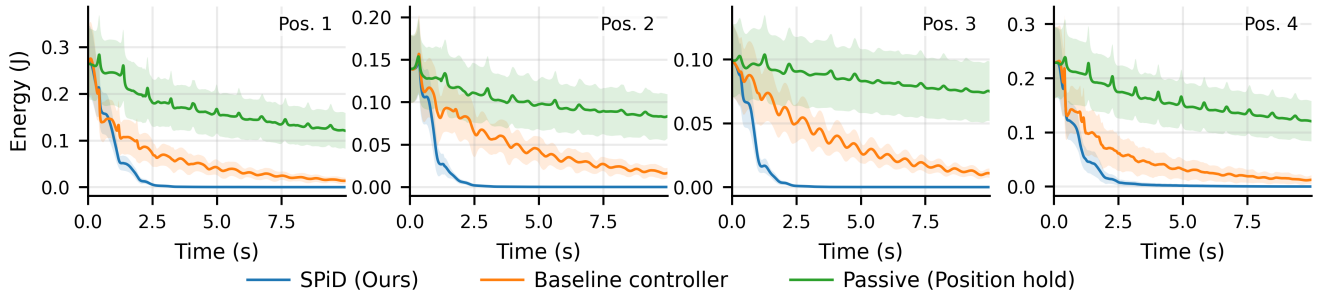


Fig. 7: **Simulation results.** Performance of the three controllers under 4 different initial rope positions. Each curve represents the mean energy profile over  $5^3$  different rope settings. Shaded regions show one standard deviation. SPiD achieves the fastest and most stable convergence, while the baseline controller exhibits oscillations in some cases.

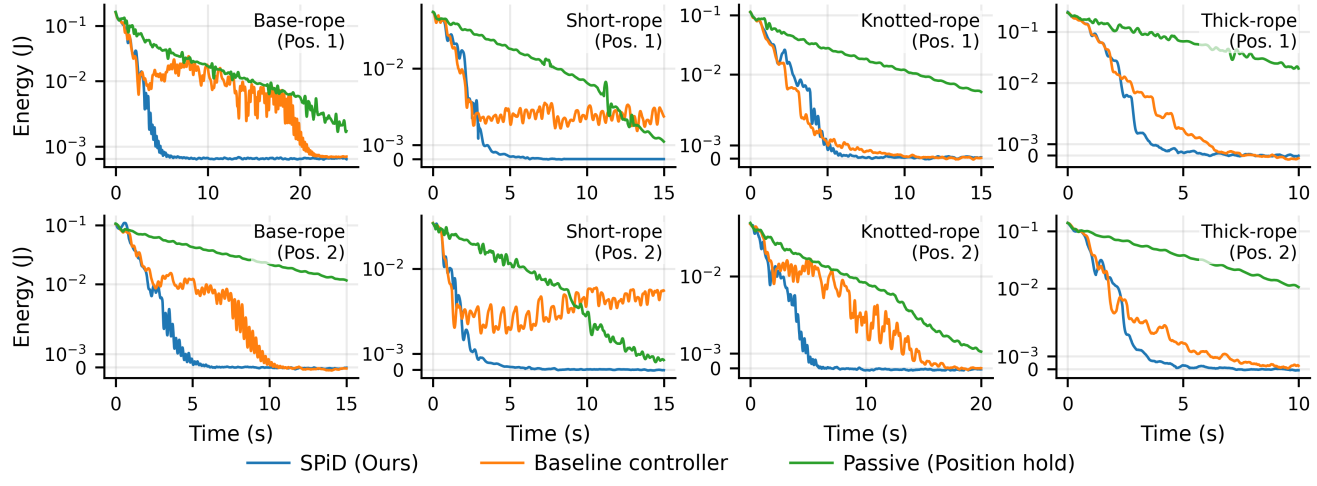


Fig. 8: **Real-world results.** Comparative experiments of three controllers were conducted on four different ropes under two initial positions. Our controller consistently achieved the best performance across all scenarios, demonstrating both the effectiveness and generalization capability of the proposed algorithm.

TABLE II: Rope stabilization time (s) in real-world experiments. “–” indicates that the rope did not reach the stabilization condition within the experiment duration.

	Rope type	Passive	Baseline	SPiD (Ours)
Pos.1	Base-rope	–	19.50	<b>4.07</b>
	Short-rope	–	–	<b>3.69</b>
	Knotted-rope	–	<b>4.89</b>	<b>4.77</b>
	Thick-rope	–	4.97	<b>2.92</b>
Pos.2	Base-rope	–	9.20	<b>4.23</b>
	Short-rope	–	–	<b>3.58</b>
	Knotted-rope	–	14.05	<b>5.03</b>
	Thick-rope	–	5.29	<b>3.24</b>

Panda robotic arm equipped with a Franka Hand gripper, which grasps the top end of the rope. The desired velocity of the robot end-effector is updated at 100Hz, while the velocity controller runs at 1000Hz. Rope segment positions are tracked at 100 Hz using the OptiTrack motion capture system consisting of 12 infrared cameras. For this purpose, we attached 9 equally spaced reflective markers along the rope. The velocity of each marker is then estimated by differentiating the position data, followed by filtering to reduce noise, thereby reconstructing the full state of the rope.

To evaluate the generalization capability of the proposed algorithm, four types of ropes are used, as shown in Fig. 6b: *Base-rope* – a cotton rope (16g/m, 80cm in length), also used for system identification; *Short-rope* – a shorter version of the base-rope (16g/m, 60cm in length); *Knotted-rope* – the base-rope tied with five knots (80cm after tying); *Thick-rope* – a thicker rope (40g/m, 80cm in length). To enrich the dynamic characteristics of the ropes, additional weights of 15g, 7g, 7g, and 15g are attached to the tips of the four ropes, respectively. For each rope, two different initial positions are selected for testing, as illustrated in Fig. 6c.

**Results.** The real-world experiment results are shown in Fig. 8, for four types of ropes (Fig. 6b) and two initial positions (Fig. 6c). For the base-rope, our controller quickly stabilizes the rope, while the baseline controller experiences oscillations before eventually settling down, although it still performs significantly better than the passive case. This oscillation behavior arises because the baseline controller is derived from a simplified rope model, where the rope is approximated as a double pendulum. In reality, however, the rope exhibits more complex dynamics, and this model mismatch leads to degraded performance. In contrast, our controller explicitly accounts for the rope’s dynamic characteristics, resulting in faster and more stable control.

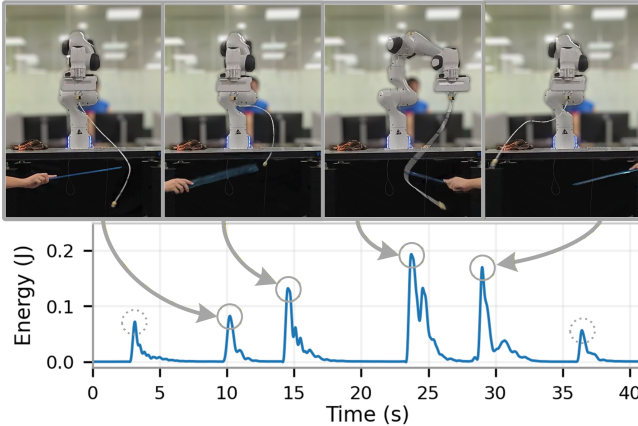


Fig. 9: **Robustness to external disturbances.** The rope is manually disturbed to evaluate system robustness. The corresponding energy profile and key snapshots of the experiment are presented. The system rapidly dissipated the injected energy and achieved stability.

When using a shorter rope, our method remains stable, whereas the baseline starts to oscillate after a certain point — even performing worse than the passive case. This occurs because a shorter rope produces a larger swinging angle for the same top-end displacement, and such “overshooting” prevents convergence. Consequently, the baseline optimized for long ropes fails to generalize to shorter ones, while our method remains effective across different rope lengths.

For the knotted rope, the baseline achieves performance similar to our controller in the *pos. 1* case, but it again exhibits oscillations in the *pos. 2* case and takes longer to reach stability compared to the base-rope experiment. Finally, for the thick rope, our controller still stabilizes the rope faster than both the baseline and the passive cases.

Our controller consistently achieves rope stabilization in the shortest time across all scenarios as reported in Table II. Overall, our method demonstrates superior control performance and generalization capability across all scenarios.

**Robustness to external disturbances.** To evaluate the robustness of SPiD, we manually disturb the base-rope at arbitrary points and directions. Upon the application of external disturbances, the rope state rapidly transitions from a static condition to fast motion. The controller responds promptly and re-stabilizes the rope in a closed-loop manner. Fig. 9 shows key snapshots of the experiment. From the energy profile, it can be observed that our controller rapidly dissipates injected energy and achieves fast re-stabilization of the system.

### C. Markerless rope stabilization

We evaluate our markerless rope perception method in three sections. We start by presenting our preliminary evaluation of the pretrained segmentation models in Sec. V-C.1. Then, we evaluate performance and limitations of the markerless perception method on our main task, firstly, by comparing it to the marker-based perception, and secondly, by running a rope stabilization control experiment without

TABLE III: Quantitative comparison of rope segmentation performance and runtime.

Method	Precision	Recall	F1-score	FPS
Grounded-SAM	<b>0.8703</b>	0.8819	<b>0.8743</b>	0.41
Grounded-Mobile-SAM	0.6001	0.8727	0.6512	2.45
Fine-tuned YOLOv11-seg	<b>0.8605</b>	<b>0.9434</b>	<b>0.8980</b>	<b>39.80</b>

markers.

*1) Rope detection and segmentation:* In this section we compare different detection and segmentation approaches for rope tracking, as introduced in Sec. IV-B. We compare three approaches for this problem: (1) *Grounded-SAM* combines Grounding DINO [41] for detecting object bounding box (prompt: “rope”) and SAM [37] for pixel-wise segmentation; (2) *Grounded-Mobile-SAM* combines Grounding DINO with Mobile-SAM [42] that replaces SAM’s large image encoder with a lightweight encoder designed for faster inference; (3) *Fine-tuned YOLOv11-seg* [43] detects the object and segments it through a unified model that is fine-tuned with our dataset.

**Data collection and fine-tuning.** A rope dataset was collected using an Intel RealSense D435i RGB-D camera. RGB images were captured at 60 FPS to cover a wide range of dynamic rope configurations. The dataset includes four different ropes with varying colors (blue, green, white, and black), lengths, and thicknesses. Data were recorded under diverse conditions, including multiple backgrounds, illumination variations, and dynamic motions, to improve robustness and generalization. The final dataset consists of 12,400 images for training and 2,200 images for validation and testing. To better capture the thin ropes, a high resolution images ( $960 \times 960$  px) were used during both training and inference. Pixel-level annotations were initially generated by Grounded-SAM’s text-prompt-based detection and segmentation. These masks were then manually reviewed and refined using a custom graphical annotation interface and the CVAT<sup>2</sup> annotation tool.

The YOLOv11-seg model is fine-tuned for 100 epochs with cosine learning-rate decay and mild weight regularization to improve segmentation stability. During inference, each RGB frame is resized to the network input resolution and processed in real time on an NVIDIA RTX 2000 Ada Generation GPU with 8 GB of memory.

**Results.** Table III presents the precision, recall, and F1-score and average frames per second (FPS) of each approach on the same test split of the collected dataset under identical hardware conditions.

The experimental results highlight the limitations of prompt-based foundation models for real-time rope perception and demonstrate the advantages of a task-specific, fine-tuned segmentation model. Although Grounded-Mobile-SAM improves inference speed through a lightweight image encoder, the end-to-end latency is still dominated by GroundingDINO, resulting in insufficient frame rates for real-time deployment. Furthermore, it achieves lower precision and

<sup>2</sup>CVAT: Computer Vision Annotation Tool, <https://www.cvcat.ai>

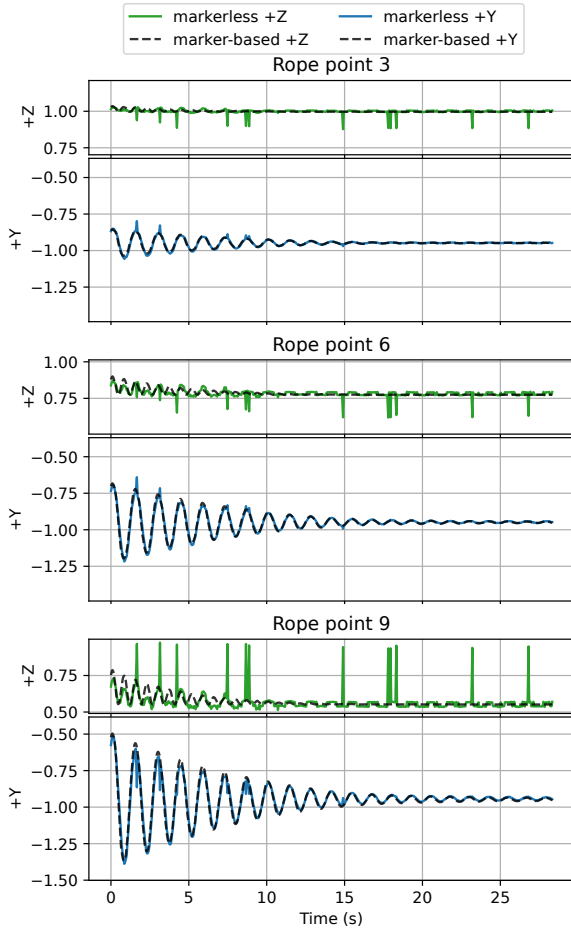


Fig. 10: Comparison of markerless and marker-based perception, shown for rope points 3, 6 and 9 on YZ-axes.

F1-score due to reduced model capacity. The fine-tuned YOLOv11-seg model overcomes these limitations by jointly performing detection and segmentation in a single forward pass. This unified architecture significantly reduces inference latency while maintaining high segmentation accuracy, with the additional cost of data collection and fine-tuning.

2) *Comparison to marker-based perception:* In this experiment, we let a rope swing for 28 s while tracking it by both the marker-based and markerless perception systems that are described in Section IV. We use the marker-based tracking positions as our reference to assess the accuracy of the markerless tracking method. Marker-based tracking is based on OptiTrack system that uses multiple high-frequency cameras and reflective markers to achieve high accuracy tracking. Markerless tracking is done using a single Intel RealSense camera that is more affordable and portable, however, it produces less accurate results at a lower frequency.

The whole markerless perception pipeline, including the segmentation and point splitting, publishes point clouds at 22 Hz frequency on average, as compared to 100 Hz of marker-based perception. After orienting the reference frames by manual calibration and removing mean bias for each axis, the RMSE between the markerless and marker-based tracking over all points and YZ-axes is 2.381 cm. We plot the tracked

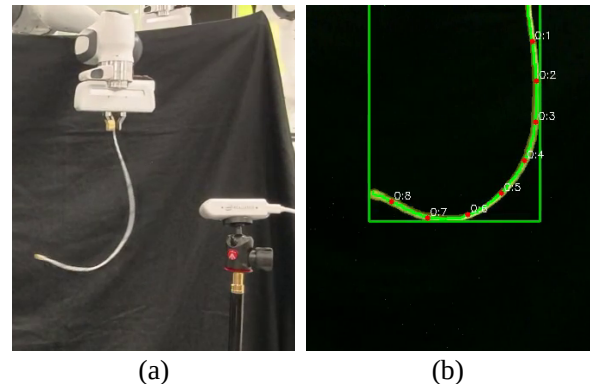


Fig. 11: **Markerless rope stabilization.** (a) Experiment setup with a single RGB camera. (b) Annotated camera view with the detection box, segmentation mask and equally split nodes.

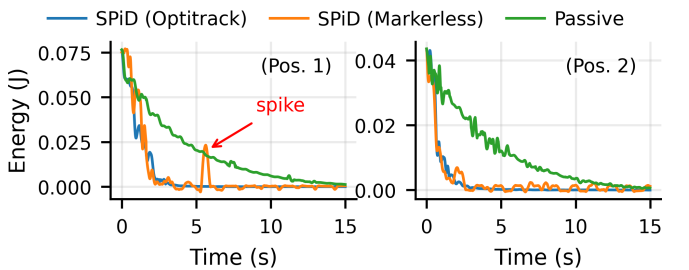


Fig. 12: **Comparison of control performance under markerless perception.** SPiD maintains similar performance under coarse markerless perception. The oscillations are due to the perception rather than real rope motion, including the annotated spike.

positions of 3 rope points in Fig. 10. As seen on the figure, z-axis (altitude) contains more error. This stems from the momentary shifts that are caused by jumps in rope splitting. The y-axis shows higher accuracy, enabling the rope stabilization control.

Unlike the marker-based approach that is 3-D, the markerless system tracks rope segments in 2-D. We also tested 3-D markerless tracking by sampling the depth values for the segmented rope points as provided by the RGB-D camera. However, this data proved too noisy to be useful even with filtering efforts.

3) *Control experiment:* We validate the feasibility of our controller in a markerless single camera setup as shown in Fig. 11. We used a simple background as the segmentation method can easily confuse parts of the background with a white rope. Another limitation of this approach is the field-of-view. As the camera goes farther than the rope, it becomes harder to segment a thin rope. On the other hand, getting closer constrains the area in which the rope can be observed.

We conducted the stabilization experiments with *short-rope* for two initial positions (Fig. 6). We present the energy plot of *markerless SPiD* in Fig. 12, comparing it to the results obtained in the previous experiment. Please note that the remaining spikes in the energy plot are due to the spikes in perception output as seen in Fig. 10, rather than rope

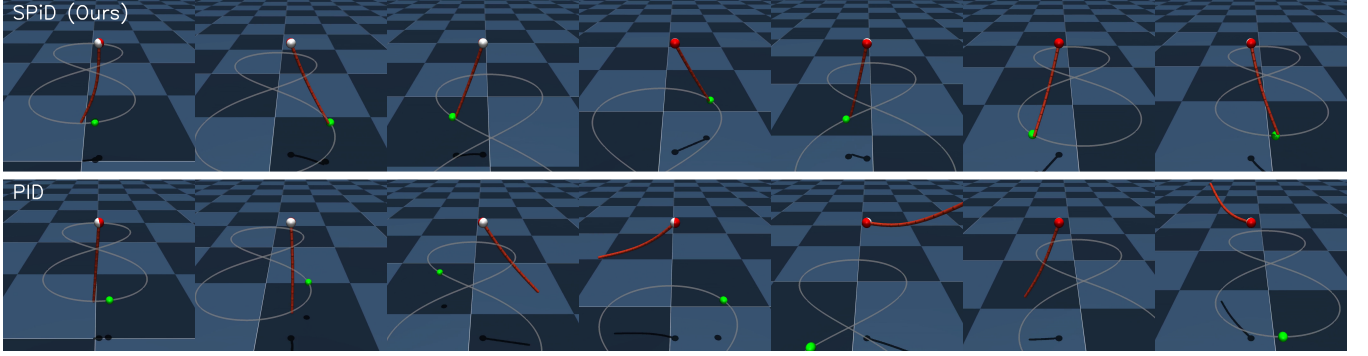


Fig. 13: Snapshots of rope trajectory tracking on the 2.5s Lemniscate. Top: SPiD (ours); Bottom: PID baseline.

TABLE IV: Mean and standard deviation of tracking error (in meters) over different target trajectories and durations.

Method	Sinusoid		Egg		Lemniscate	
	$T = 2.5\text{s}$	$T = 5.0\text{s}$	$T = 2.5\text{s}$	$T = 5.0\text{s}$	$T = 2.5\text{s}$	$T = 5.0\text{s}$
PID	$0.1617 \pm 0.0006$	$0.0398 \pm 0.0014$	$0.1470 \pm 0.0023$	$0.0392 \pm 0.0012$	$0.3082 \pm 0.0005$	$0.0984 \pm 0.0020$
SPiD (Ours)	<b><math>0.0299 \pm 0.0004</math></b>	<b><math>0.0134 \pm 0.0003</math></b>	<b><math>0.0275 \pm 0.0004</math></b>	<b><math>0.0109 \pm 0.0002</math></b>	<b><math>0.0221 \pm 0.0005</math></b>	<b><math>0.0127 \pm 0.0001</math></b>

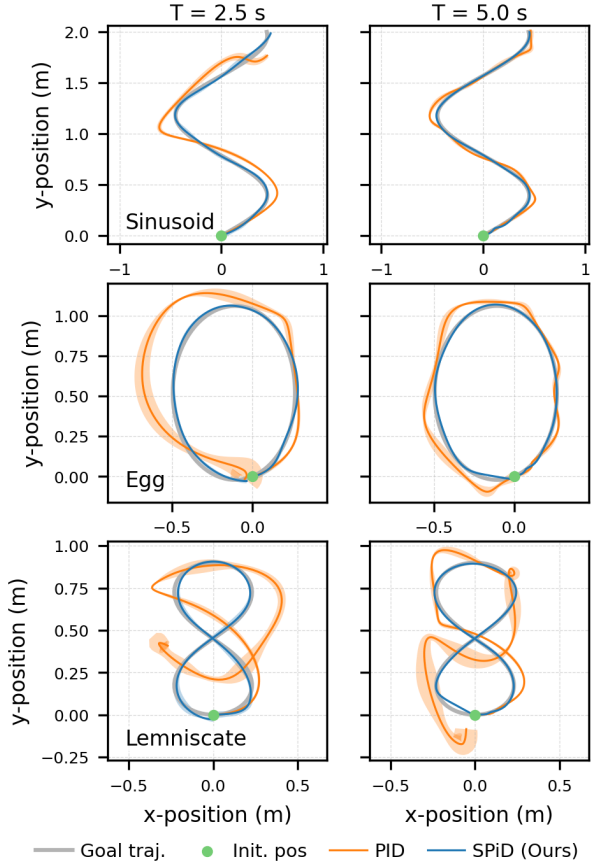


Fig. 14: Trajectory tracking results. Three target trajectories under two different durations are evaluated. For each setting, results are averaged over  $5^3$  rope models with different physical parameters, with solid lines showing the mean tracked trajectories and shaded regions indicating  $\pm 3$  std measured orthogonally to the mean trajectory. Our method achieves more accurate tracking compared to the baseline.

motion. Despite the limitations of the perception system, we were able to achieve equally swift rope stabilization without fine-tuning our controller. This is made possible by the robustness of our controller and a fairly accurate rope perception method.

#### D. Generalization to rope trajectory tracking

To demonstrate the generality of SPiD, we apply the same approach to a new task in simulation. The rope trajectory tracking task requires manipulating the top end of the rope such that its bottom end follows a desired trajectory. Compared to the rope stabilization task, only two aspects need to be reformulated:

- The loss function is changed from the rope energy to the distance between the rope tip trajectory and the target trajectory.
- A short segment of the future target trajectory is included in the controller input, so that it learns to act in a predictive manner.

##### 1) Task formulation:

**Task specification.** In this task, the task specification  $\mathbf{G}$  includes the target trajectory, because this information is necessary to define the loss function and achieve predictive behavior. The target trajectory is represented as  $\mathbf{G} = \{\mathbf{g}_{\text{goal}}^t\}_{t=1 \dots T}$ , where  $\mathbf{g}_{\text{goal}}^t \in \mathbb{R}^3$  denotes the target position at time step  $t$ . Instead of feeding the entire trajectory  $\mathbf{G}$  into the controller, we concatenate the current rope state with the current target point and the next 40 target points.

**Loss function.** Given the initial state  $\mathbf{X}^0$ , the rope evolves over time under the action of the controller, producing a sequence of states  $\{\mathbf{X}^t\}_{t=1 \dots T}$ . In the trajectory tracking task, we only require the rope tip to stably track the target trajectory, without considering the trajectories of the other rope nodes. Therefore, we extract the position of the rope tip  $\mathbf{p}_N^t$  from  $\mathbf{X}^t$  and define the tracking loss based on its

distance to the target position  $\mathbf{g}_{\text{goal}}^t$  as

$$\mathbf{L}_{\text{task}}(\{\mathbf{X}^t\}_{t=1}^T, \mathbf{G}) = \sum_{t=1}^T \gamma^{T-t} \cdot \left\| \mathbf{p}_N^t - \mathbf{g}_{\text{goal}}^t \right\|_2^2, \quad (19)$$

where  $\gamma \in (0, 1]$  is a discount factor that places greater emphasis on tracking accuracy at later time steps.

**Metrics.** We evaluate the tracking performance by the average Euclidean distance between the executed trajectory and the target trajectory. Specifically, the tracking error is defined as

$$e_{\text{track}} = \frac{1}{T} \sum_{t=1}^T \left\| \mathbf{p}_N^t - \mathbf{g}_{\text{goal}}^t \right\|_2, \quad (20)$$

where a smaller value indicates better tracking accuracy.

*2) Baseline controller:* For comparison, we adopt a PID controller as the baseline. The control error is defined as the positional deviation between the rope tip and the target point. For each target trajectory and each trajectory duration, a separate set of PID gains is independently tuned, resulting in a total of six parameter sets. In contrast, the SPiD employs a single fixed policy across all trajectories and durations.

### 3) Simulation experiments:

**Setup.** The simulation experiments are conducted in MuJoCo using a 30cm rope model composed of 12 serially connected rigid segments. We reuse the previously identified physics model to train the controller, while reducing the number of mass points  $N$  to 7. The rope is manipulated by controlling the velocity of its top end in the 3-D space at a control frequency of 100Hz. We evaluate the performance of the proposed method on three different target trajectories, namely Sinusoid, Egg, and Lemniscate trajectories, as illustrated in Fig. 14. The total path lengths of the three target trajectories are 3.13m, 2.92m, and 2.77m, respectively.

To examine tracking performance under different motion speeds, we consider two trajectory durations, 2.5s and 5.0s. For the shorter duration of 2.5s, the maximum velocities along the sinusoid, egg-shaped, and lemniscate trajectories reach 1.98m/s, 1.79m/s, and 1.47m/s, respectively. Furthermore, following the same setup as in the rope stabilization task, we sample 5<sup>3</sup> rope models with different physical properties to evaluate the generalization aspect.

**Results.** The tracking results are shown in Fig. 14. Our method consistently achieves accurate tracking performance across different trajectories, time durations, and rope properties. In contrast, the baseline method only achieves reasonable performance on slow ( $T = 5.0$ ) and simple trajectories (e.g., the sinusoid-egg case), fails to accurately track the Lemniscate trajectory, and exhibits significantly larger tracking variance across different rope properties in all cases. Fig. 13 further presents representative tracking snapshots for the 2.5s Lemniscate trajectory. Finally, the quantitative results are summarized in Table IV, where our method achieves substantially lower mean error and standard deviation in all cases compared with the baseline method.

## VI. CONCLUSIONS

This paper proposed SPiD, a physics-informed self-supervised learning framework for dynamic manipulation of

deformable linear objects. The effectiveness, generalizability, and robustness of SPiD were demonstrated on an online rope stabilization task through extensive experiments in both simulation and the real world, even under coarse markerless perception. Furthermore, the same framework was extended to a trajectory tracking task with only minimal modifications. Across both tasks, the proposed method achieved superior performance over baseline approaches through improved physical modeling and the augmented self-supervised training strategy. Our dynamics model demonstrated increased accuracy in rope motion prediction with the contribution of the newly introduced damping terms. Furthermore, it enabled the real-time rope manipulation with a neural network controller. We were able to train a highly robust and generalizable controller with limited data without expert demonstrations, owing to the proposed augmented self-supervised learning strategy, including a novel self-supervised DAgger variant.

However, our work is not without limitations. The current model is applied to objects with a one-dimensional topology, such as ropes, and has not yet been validated on higher-dimensional deformable objects. While we expect the approach to scale in a straightforward manner, future work will focus on extending the model to two- and three-dimensional deformable objects, such as cloth or sponge-like materials, and evaluating the proposed approach on additional challenging tasks.

## REFERENCES

- [1] H. Yin, A. Varava, and D. Kragic, “Modeling, learning, perception, and control methods for deformable object manipulation,” *Science Robotics*, vol. 6, no. 54, p. eabd8803, 2021.
- [2] C. Chi, B. Burchfiel, E. Cousineau, S. Feng, and S. Song, “Iterative residual policy: for goal-conditioned dynamic manipulation of deformable objects,” *The International Journal of Robotics Research*, vol. 43, no. 4, pp. 389–404, 2024.
- [3] M. T. Mason and K. M. Lynch, “Dynamic manipulation,” in *Proceedings of 1993 IEEE/RSJ International Conference on Intelligent Robots and Systems (IROS’93)*, vol. 1. IEEE, 1993, pp. 152–159.
- [4] K. Zhang, B. Li, K. Hauser, and Y. Li, “Particle-grid neural dynamics for learning deformable object models from rgb-d videos,” *arXiv preprint arXiv:2506.15680*, 2025.
- [5] B. Shen, Z. Jiang, C. B. Choy, S. Savarese, L. J. Guibas, A. Anandkumar, and Y. Zhu, “Acid: Action-conditional implicit visual dynamics for deformable object manipulation,” in *Robotics: Science and Systems*, 2022.
- [6] G. Salhotra, I.-C. A. Liu, M. Dominguez-Kuhne, and G. S. Sukhatme, “Learning deformable object manipulation from expert demonstrations,” *IEEE Robotics and Automation Letters*, vol. 7, no. 4, pp. 8775–8782, 2022.
- [7] J. B. Rawlings, D. Q. Mayne, M. Diehl *et al.*, *Model predictive control: theory, computation, and design*. Nob Hill Publishing Madison, WI, 2020, vol. 2.
- [8] D. Mayne, “Nonlinear model predictive control: Challenges and opportunities,” *Nonlinear model predictive control*, pp. 23–44, 2000.
- [9] N. Lv, J. Liu, X. Ding, J. Liu, H. Lin, and J. Ma, “Physically based real-time interactive assembly simulation of cable harness,” *Journal of Manufacturing Systems*, vol. 43, pp. 385–399, 2017.
- [10] H. Chen, Y. Fang, and N. Sun, “A swing constrained time-optimal trajectory planning strategy for double pendulum crane systems,” *Nonlinear Dynamics*, vol. 89, no. 2, pp. 1513–1524, 2017.
- [11] Y. Zhao, Y. Fang, S. Wu, and J. Lin, “Robust antiswing control for offshore boom cranes subject to disturbances on both actuated and unactuated states,” *IEEE/ASME Transactions on Mechatronics*, 2024.
- [12] Z. Liu, Y. Fu, N. Sun, T. Yang, and Y. Fang, “Collaborative antiswing hoisting control for dual rotary cranes with motion constraints,” *IEEE Transactions on Industrial Informatics*, vol. 18, no. 9, pp. 6120–6130, 2021.

- [13] I. Palunko, R. Fierro, and P. Cruz, “Trajectory generation for swing-free maneuvers of a quadrotor with suspended payload: A dynamic programming approach,” in *2012 IEEE international conference on robotics and automation*. IEEE, 2012, pp. 2691–2697.
- [14] Y. Wu, P. Zhao, D. Liang, and J. Dong, “A learning-based anti-swing trajectory refinement approach for uavs with cable-suspended payload without offline training,” *IEEE Transactions on Intelligent Vehicles*, 2024.
- [15] H. M. Omar and S. M. Mukras, “Integrating anti-swing controller with px4 autopilot for quadrotor with suspended load,” *Journal of mechanical science and technology*, vol. 36, no. 3, pp. 1511–1519, 2022.
- [16] M. Benosman, “Lyapunov-based control of the sway dynamics for elevator ropes,” *IEEE Transactions on Control Systems Technology*, vol. 22, no. 5, pp. 1855–1863, 2014.
- [17] D. R. Haumann and R. E. Parent, “The behavioral test-bed: Obtaining complex behavior from simple rules,” *The Visual Computer*, vol. 4, no. 6, pp. 332–347, 1988.
- [18] L. Zhong, H.-X. Yu, J. Wu, and Y. Li, “Reconstruction and simulation of elastic objects with spring-mass 3d gaussians,” in *European Conference on Computer Vision*. Springer, 2024, pp. 407–423.
- [19] M. Macklin, M. Müller, N. Chentanez, and T.-Y. Kim, “Unified particle physics for real-time applications,” *ACM Transactions on Graphics (TOG)*, vol. 33, no. 4, pp. 1–12, 2014.
- [20] P. Guler, K. Pauwels, A. Pieropan, H. Kjellström, and D. Kragic, “Estimating the deformability of elastic materials using optical flow and position-based dynamics,” in *2015 IEEE-RAS 15th International Conference on Humanoid Robots (Humanoids)*. IEEE, 2015, pp. 965–971.
- [21] L. Greco and M. Cuomo, “B-spline interpolation of kirchhoff-love space rods,” *Computer Methods in Applied Mechanics and Engineering*, vol. 256, pp. 251–269, 2013.
- [22] M. Bergou, M. Wardetzky, S. Robinson, B. Audoly, and E. Grinspun, “Discrete elastic rods,” in *ACM SIGGRAPH 2008 papers*. Association for Computing Machinery, 2008, pp. 1–12.
- [23] N. Lv, J. Liu, H. Xia, J. Ma, and X. Yang, “A review of techniques for modeling flexible cables,” *Computer-Aided Design*, vol. 122, p. 102826, 2020.
- [24] Y. Deng, X. Wang, and L. Chen, “Learning visual-based deformable object rearrangement with local graph neural networks,” *Complex & Intelligent Systems*, vol. 9, no. 5, pp. 5923–5936, 2023.
- [25] K. Zhang, B. Li, K. Hauser, and Y. Li, “Adaptigraph: Material-adaptive graph-based neural dynamics for robotic manipulation,” *arXiv preprint arXiv:2407.07889*, 2024.
- [26] C. Li, Z. Ai, T. Wu, X. Li, W. Ding, and H. Xu, “Deformnet: Latent space modeling and dynamics prediction for deformable object manipulation,” in *2024 IEEE International Conference on Robotics and Automation (ICRA)*. IEEE, 2024, pp. 14 770–14 776.
- [27] M. Yu, K. Lv, H. Zhong, S. Song, and X. Li, “Global model learning for large deformation control of elastic deformable linear objects: An efficient and adaptive approach,” *IEEE Transactions on Robotics*, vol. 39, no. 1, pp. 417–436, 2022.
- [28] P. Sundaresan, J. Grannen, B. Thananjeyan, A. Balakrishna, M. Laskey, K. Stone, J. E. Gonzalez, and K. Goldberg, “Learning rope manipulation policies using dense object descriptors trained on synthetic depth data,” in *2020 IEEE International Conference on Robotics and Automation (ICRA)*. IEEE, 2020, pp. 9411–9418.
- [29] R. Hoque, D. Seita, A. Balakrishna, A. Ganapathi, A. K. Tanwani, N. Jamali, K. Yamane, S. Iba, and K. Goldberg, “Visuospatial fore-sight for multi-step, multi-task fabric manipulation,” *arXiv preprint arXiv:2003.09044*, 2020.
- [30] J. Schulman, J. Ho, C. Lee, and P. Abbeel, “Learning from demonstrations through the use of non-rigid registration,” in *Robotics Research: The 16th International Symposium ISRR*. Springer, 2016, pp. 339–354.
- [31] M. Lippi, P. Poklukar, M. C. Welle, A. Varava, H. Yin, A. Marino, and D. Kragic, “Latent space roadmap for visual action planning of deformable and rigid object manipulation,” in *2020 IEEE/RSJ International Conference on Intelligent Robots and Systems (IROS)*. IEEE, 2020, pp. 5619–5626.
- [32] H. Chen, J. Xu, L. Sheng, T. Ji, S. Liu, Y. Li, and K. Driggs-Campbell, “Learning coordinated bimanual manipulation policies using state diffusion and inverse dynamics models,” in *2025 IEEE International Conference on Robotics and Automation (ICRA)*. IEEE, 2025, pp. 5644–5651.
- [33] G. Lan, Y. Yang, A. T. Mathew, F. Nie, R. Wang, X. Li, F. Renda, and B. Zhao, “Dynamic manipulation of deformable objects in 3d: Simulation, benchmark and learning strategy,” *arXiv preprint arXiv:2505.17434*, 2025.
- [34] V. Lim, H. Huang, L. Y. Chen, J. Wang, J. Ichnowski, D. Seita, M. Laskey, and K. Goldberg, “Real2sim2real: Self-supervised learning of physical single-step dynamic actions for planar robot casting,” in *2022 International Conference on Robotics and Automation (ICRA)*. IEEE, 2022, pp. 8282–8289.
- [35] A. Nair, D. Chen, P. Agrawal, P. Isola, P. Abbeel, J. Malik, and S. Levine, “Combining self-supervised learning and imitation for vision-based rope manipulation,” in *2017 IEEE international conference on robotics and automation (ICRA)*. IEEE, 2017, pp. 2146–2153.
- [36] J. Schulman, A. Lee, J. Ho, and P. Abbeel, “Tracking deformable objects with point clouds,” in *2013 IEEE International Conference on Robotics and Automation*. IEEE, 2013, pp. 1130–1137.
- [37] A. Kirillov, E. Mintun, N. Ravi, H. Mao, C. Rolland, L. Gustafson, T. Xiao, S. Whitehead, A. C. Berg, W.-Y. Lo, P. Dollar, and R. Girshick, “Segment anything,” in *Proceedings of the IEEE/CVF International Conference on Computer Vision (ICCV)*, October 2023, pp. 4015–4026.
- [38] A. Theetten, L. Grisoni, C. Andriot, and B. Barsky, “Geometrically exact dynamic splines,” *Computer-Aided Design*, vol. 40, no. 1, pp. 35–48, 2008.
- [39] P. P. Valentini and E. Pennestrì, “Modeling elastic beams using dynamic splines,” *Multibody system dynamics*, vol. 25, no. 3, pp. 271–284, 2011.
- [40] S. Ross, G. Gordon, and D. Bagnell, “A reduction of imitation learning and structured prediction to no-regret online learning,” in *Proceedings of the fourteenth international conference on artificial intelligence and statistics*. JMLR Workshop and Conference Proceedings, 2011, pp. 627–635.
- [41] S. Liu, Z. Zeng, T. Ren, F. Li, H. Zhang, J. Yang, Q. Jiang, C. Li, J. Yang, H. Su *et al.*, “Grounding dino: Marrying dino with grounded pre-training for open-set object detection,” in *European conference on computer vision*. Springer, 2024, pp. 38–55.
- [42] C. Zhang, D. Han, Y. Qiao, J. U. Kim, S.-H. Bae, S. Lee, and C. S. Hong, “Faster segment anything: Towards lightweight sam for mobile applications,” *arXiv preprint arXiv:2306.14289*, 2023.
- [43] Ultralytics, “Ultralytics yolov11,” <https://github.com/ultralytics/ultralytics>, 2024.